ECS Journal of Solid State
Science and Technology

The Electrochemical Society
Advancing solid state & electrochemical science & technology

Damage Recovery and Dopant Diffusion in Si and Sn Ion Implanted β-Ga_2O_3

To cite this article: Marko J. Tadjer *et al* 2019 *ECS J. Solid State Sci. Technol.* **8** Q3133

ECS Journal of Solid State Science and Technology, **8** (7) Q3133-Q3139 (2019)

JSS FOCUS ISSUE ON GALLIUM OXIDE BASED MATERIALS AND DEVICES

Damage Recovery and Dopant Diffusion in Si and Sn Ion Implanted β-Ga_2O_3

Marko J. Tadjer,[1,z] Chaker Fares,[2,*] Nadeemullah A. Mahadik,[1] Jaime A. Freitas Jr.,[1] David Smith,[3] Ribhu Sharma,[4] Mark E. Law,[4,] Fan Ren,[2,***] S. J. Pearton,[5,***] and A. Kuramata[6]**

[1]*U.S. Naval Research Laboratory, Washington, DC 20375, USA*
[2]*Department of Chemical Engineering, University of Florida, Gainesville, Florida 32611, USA*
[3]*Department of Physics, University of Arizona, Tempe, Arizona, USA*
[4]*Department of Electrical and Computer Engineering, University of Florida, Gainesville, Florida 32611, USA*
[5]*Department of Materials Science and Engineering, University of Florida, Gainesville, Florida 32611, USA*
[6]*Tamura Corp. and Novel Crystal Technology, Sayama-city, Saitama 350-1328, Japan*

The commonly used n-type dopants, Si and Sn, were implanted into bulk (−201) β-Ga_2O_3 over a 2 order of magnitude dose range and annealed at temperatures from 1000–1150°C. The original lattice parameters were restored by annealing at 1150°C for the highest dose Si implants, while only partial recovery was observed in Sn implanted samples. The Sn implanted samples had overall lower lattice parameters compared to the Si implanted samples, indicating that Sn generates tensile strain in the Ga_2O_3 lattice. The rocking curve FWHM was observed to increase with the annealing process, indicating that the annealing process does not improve the crystal quality. Transmission electron microscopy showed removal of the end-of-range lattice damage after 1150°C anneals of the heaviest implanted species, Sn. Cathodoluminescence at 5K showed recovery of intensity of the common UV band around 3.2 eV after annealing. Secondary Ion Mass Spectrometry profiling showed the presence of concentration-dependent diffusion of both Si and Sn, with values for diffusivity at 1150°C of 9.5×10^{-13} cm.s^{-1} for Si and 1.7×10^{-13} cm.s^{-1} for Sn obtained by fitting through the FLOOPS simulation package.

[DOI: 10.1149/2.0271907jss]

Manuscript submitted February 7, 2019; revised manuscript received March 4, 2019. Published March 13, 2019. *This paper is part of the JSS Focus Issue on Gallium Oxide Based Materials and Devices.*

The β-polymorph of Ga_2O_3 is of interest for power electronics and solar blind UV detectors due its wide bandgap (∼4.85 eV) and high critical field (6–8 MV/cm). The availability of high-quality large area and low cost wafers,[1–16] especially those grown by the edge-defined film-fed growth (EFG) method[6] in combination with these attractive properties have potentially positioned β-Ga_2O_3 to supplement the more established wide bandgap semiconductors, SiC and GaN, in compact, high power density converters for power switching applications.[3,4,7,8,11,12] In addition to the progress in bulk growth, there is now the capability to grow high quality epilayers with controlled net free-electron concentrations in the range 10^{15}–10^{19} cm^{-3} using shallow Si, Ge, and Sn donors.[1,5,9,10,14,15] In Molecular Beam Epitaxy, Sn and Ge are typically employed for n-type doping.[5,10,14] Sn is used in mist-Chemical Vapor Deposition,[3,15] while Si and Sn are used in Metal Organic Chemical Vapor Deposition and Pulsed Laser Deposition.[1,5] Si is a substitutional (Si_{Ga}) shallow donor (16–30 meV) and may be responsible for much of the prevailing n-type conductivity in Ga_2O_3.[2,3,6,16]

Ion implantation has not been extensively studied in Ga_2O_3,[11,17–21] with early reports of use of Si for doping the channel and the contact regions.[11] Ohmic contacts were formed to Ga_2O_3 using implanted Si to form n$^+$ regions under the contact metal.[11,19] The implants were activated by 950°C rapid-thermal annealing. ohmic contacts made to these Si-implanted layers using Ti/Au metallization showed a specific contact resistivity of 4.6×10^{-6} Ω.cm^2, using a three-step contact process (BCl_3/Ar etch, Ti/Au metal liftoff, 1 min. 450°C RTA).[11] The implantation of Mg (a deep acceptor) and N[21] have been used for selectively defining highly resistive regions for current-blocking in vertical transistors[21] and inter-device isolation.[18] N was found to exhibit smaller diffusion coefficients than Mg, thus enabling the use of higher annealing temperatures to maximize N activation efficiency without significantly altering the impurity profile.[21] One surprising feature to date has been the high diffusivities of some of the implanted species.[21] Secondary Ion Mass Spectrometry (SIMS) depth profiles of Mg and N showed significant Mg diffusion at annealing temperatures ≥900 °C, with the as-implanted Gaussian Mg profile transformed into a box-like profile with a sharp cutoff tail and a plateau concentration stabilized at the background donor (Sn) concentration.[21] The Mg diffusion was concentration independent. By contrast, implanted N showed less significant redistribution at 1200 °C and also stabilized at the background Si concentration of 2×10^{17} cm^{-3}. In addition to implantation of electrically active dopants or device isolation species, rare earth dopants such as Eu have been implanted for producing temperature-insensitive optical emission bands.[13] Tadjer et al.[7] reported the effect of annealing ambient on non-implanted (−201) Ga_2O_3 annealed in N_2 and O_2 in order to independently quantify the effect of the annealing process on conductivity and showed lower background carrier concentrations and higher reverse breakdown voltages from diodes annealed in O_2 ambient.

Much more needs to be done to understand the damage removal and dopant diffusion characteristics of Ga_2O_3 implanted with the common n-type dopants. In this paper, samples of unintentionally doped EFG-grown (−201) β-Ga_2O_3 substrates were implanted with Si and Sn ions with multiple energies in the 30–200 keV range in order to obtain nearly-uniform profiles of 10^{18} cm^{-3}, 10^{19} cm^{-3}, and 10^{20} cm^{-3}, and subsequently processed with an activation anneal to activate the donors and remove residual implantation damage to the lattice. Samples with the highest total dose (10^{20} cm^{-3}) were characterized with X-ray diffraction (XRD), cathodoluminescence spectroscopy (CL), SIMS, and cross-section transmission electron microscopy (TEM) before and after annealing. There were clear differences in damage recovery between the lightest (Si) and heaviest (Sn) implant species. Both were found to exhibit significant diffusivity at 1150°C.

---

[*] Electrochemical Society Student Member.
[**] Electrochemical Society Member.
[***] Electrochemical Society Fellow.
[z] E-mail: marko.tadjer@nrl.navy.mil

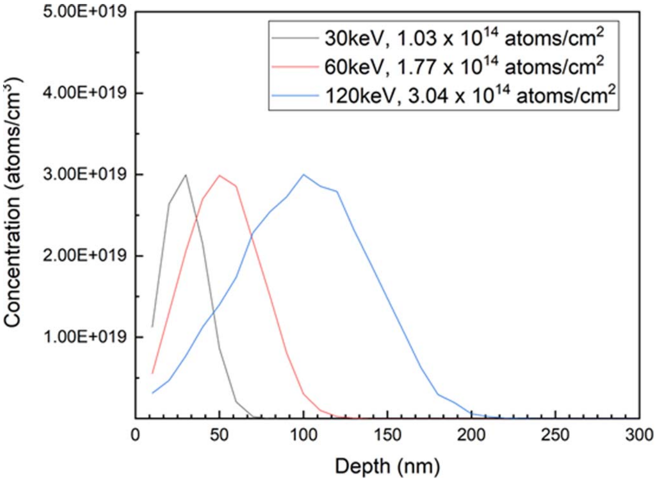

Figure 1. SRIM Simulations of Si profiles implanted into Ga_2O_3 at three different doses and energies to create an approximately uniform concentration profile.

Experimental

We used three types of samples in this experiment, obtained from Novel Crystal Technology. The first type were unintentionally doped edge-defined film-fed grown (EFG) Ga_2O_3 substrates (no epi), with room-temperature carrier concentration of 1–2 × 10^{17} cm^{-3}, as measured by electrochemical capacitance-voltage method. They had (−201) orientation, with XRD FWHM rocking curves of 20 arcsec and 25 arcsec in the [010] and [102] directions, respectively. The results and discussion section focused on experimental results from these (−201) oriented samples. The second type were Fe-doped (010) EFG Ga_2O_3 substrates. These were semi-insulating ($>10^{10}$ Ω.cm) with an X-ray diffraction full width at half maximum of up to 150 arcsec. To reach this high resistivity, the Fe concentration needs to be larger than the background due to residual donors and is typically ∼5 × 10^{18} cm^{-3}. The Fe produces a deep acceptor state near E_c-0.8 eV.[22–27] Finally, samples with ∼9 μm thick homoepitaxial Ga_2O_3 layers compensated with N and deposited on Fe-doped substrates were implanted as well. These epilayers were deposited by halide vapor phase epitaxy, with net free carrier concentration (N_D-N_A) of below 10^{14} cm^{-3} measured by capacitance-voltage measurements on lateral Schottky diodes. The uncertainly in the carrier concentration measurement was caused by the high series resistance in the capacitance-voltage measurements. The sheet resistance was ∼2 × 10^5 Ω/square, with a thermal activation energy of 0.81 eV. SIMS showed a Si concentration of ∼ 5 × 10^{15} cm^{-3} and a N concentration ∼2 × 10^{17} cm^{-3}, indicating that N acceptors compensated Si donors to create weakly n-type β-Ga_2O_3 layers.

All samples were implanted nominally at room temperature with a 7° tilt with respect to the beam normal. Si and Sn ions at multiple energies and doses were employed to obtain near-uniform concentrations of 10^{18},10^{19} or 10^{20} cm^{-3}. The specific conditions to get the 10^{20} cm^{-3} average doping concentrations were 3 × 10^{14} cm^{-2}/30 keV + 7 × 10^{14} cm^{-2}/60 keV + 10^{15} cm^{-2}/120 keV for Si and 2 × $10^{14}$$cm^{-2}$/60 keV + 3 × $10^{14}$$cm^{-2}$/100 keV + 4 × $10^{14}$$cm^{-2}$/200 keV for Sn. The doses were reduced by 1 or 2 orders of magnitude, respectively, to get the 10^{19} and 10^{18} cm^{-3} doping profiles. As an example, Fig. 1 shows for Si in the Stopping and Range of Ions in Matter (SRIM) simulations.

The samples were annealed in O_2 at temperatures between 900–1150°C. For most semiconductors, the implant activation temperature generally follows a two-thirds rule of thumb with respect to the melting point.[28] The melting temperature of Ga_2O_3 is 1793–1820°C,[1,5,29–32] so the 2/3 rule for implant activation annealing suggests temperatures in the range 1150–1250°C to achieve significant activation percentages. Activation annealing has typically been carried out at 900–1000°C for 30 min, with activation percentages approaching 60%.[11,20,21]

The choice of O_2 as the annealing ambient was based on assessing the literature and our prior experience with annealing of Ga_2O_3 substrates. Previous studies have shown that when annealed in N_2, there was no change in surface morphology of Ga_2O_3 at temperatures below 1150°C. However, the addition of hydrogen to the annealing ambient lowered the temperature at which degradation was evident.[29–32] Thermodynamic analysis showed that the dominant reactions are $Ga_2O_3(s) = Ga_2O\ (g) + O_2\ (g)$ in N_2 and $Ga_2O_3(s) + 2H_2(g) = Ga_2O(g) + 2H_2O\ (g)$ in a mixed flow of H_2 and N_2. Kuramata et al.[6] have reported that annealing Ga_2O_3 substrates in oxygen reduced the difference between donor and acceptor concentration (N_D-N_A) by about an order of magnitude. Tadjer et al.[7] reported a study of unintentionally-doped (−201) β-Ga_2O_3 with n-type background doping of 1.7 × 10^{17} cm^{-3} annealed in N_2 and O_2 for 3 hours at 1000°C and 1150°C, respectively. The carrier concentration in the N_2-annealed samples was ∼4.5 times higher than that in the O_2-annealed samples, which correlated with increased shallow donor concentration observed by electron-spin resonance.[7] While the annealing ambient affects carrier concentration near the surface of Ga_2O_3, it did so by less than a factor of 10. Furthermore the X-Ray diffraction analysis did not reveal significant structural damage caused by O annealing. Thus, choice of annealing ambient was not expected to make a significant difference in the present study since the total implantation dose among the samples spanned 2 orders of magnitude.

The TEM samples were prepared using the in situ FIB lift out technique on a Dual Beam FIB/SEM. The sample was coated with Pt prior to milling. To include more of the implanted regions, the TEM lamella thickness was left twice thicker than normal. The analysis was performed in cross-section with a FEI Tecnai TF-20 FEG/TEM operated at 200 kV in bright field and high resolution modes. Cathodoluminescence (CL) were excited with an electron beam current of 3 μA and a beam energy of 3 keV in ultra-high vacuum at 5 K and at room temperature. The CL emission, collected with a combination of f-number matching lens and mirrors, were analized by a compact fiber optic spectrometer. Secondary ion mass spectroscopy (SIMS) was performed at Evans Analytical with a magnetic sector Cameca system using a Cs^+ ion beam with 14.5 keV energy and 24° incident angle. The SIMS profiles were fitted using the FLorida Object Oriented Device, Process Simulator (FLOOPS).[33] This is a Technology Computer Aided Design (TCAD) tool used for semiconductor process and device modelling that will discretize and solve a set of partial and ordinary differential equations on a 1, 2 or 3D mesh using numerical methods such as the Finite Element Method and the Finite Volume Method.

Results and Discussion

Figure 2 shows the X-Ray diffraction rocking curves of the 10^{20} cm^{-3} Si-implanted samples before and after annealing. A small

Table I. Summary of XRD results on as-implanted and annealed Ga_2O_3 samples.

	Rocking curve FWHM (arcsecs)			Lattice parameter (Å)		
	(−201)	(−12,0,1)	(−11,1,1)	a	b	c
Si-implanted	15.5	6.9	3.8	12.2317	3.0496	5.8096
Si implanted/annealed	17.6	7.7	4.7	12.2314	3.0490	5.8058
Sn-implanted	29.1	11	5.2	12.2274	3.0116	5.8006
Sn implanted/annealed	34.5	15.5	5.4	12.2278	3.0297	5.8073

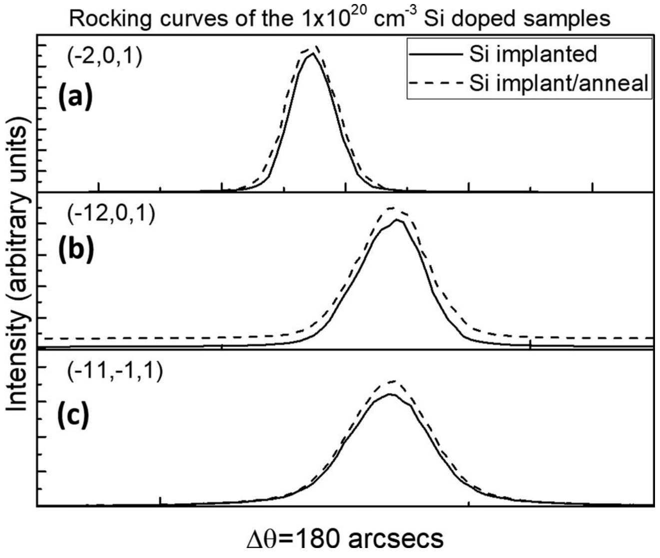

Figure 2. X-ray rocking curves of the samples implanted with Si to an average concentration of 10^{20} cm^{-3}, both before and after annealing at 1150°C.

but measurable broadening in the three measured reflections at full width half maximum was observed after annealing, as summarized in Table I and Fig. 5. Figures 3 and 4 show the high resolution Θ-2Θ scans for the 10^{20} cm^{-3} Si and Sn-implanted samples, respectively, before and after annealing. A more significant change was observed in the Sn-implanted samples, particularly in the (−11, −1, 1) reflection, where a damage peak was clearly observed before annealing. While this damage peak was partially recovered after annealing, the shift in the reflection angle remained, resulting in a measureable change in b lattice parameter for the Sn-implanted samples. The lattice parameters were obtained by recursive least squares fitting of the XRD peak positions of the three Bragg reflections collected, and summarized in Table I and Fig. 6 for both implanted species. In this plot, the y-axis intensities are shown on the same range. The change in b-parameter (010) direction for the Sn-implanted sample was only partially recovered after the 1150°C anneal. All other axis lattice parameters had very slight changes after implantation and annealing and were very close to previously reported theoretical and experimental values for the β-Ga_2O_3 lattice parameters.[34–36] The Sn-implanted samples had overall lower lattice parameters compared to the Si-implanted samples, indicating that Sn generated tensile strain in the β-Ga_2O_3 lattice. The rocking curves for the asymmetric reflections were corrected using the relation $\text{FWHM} = \text{FWHM measured}/(b)^{0.5}$, where b was the asymmetric magnification factor. The rocking curve FWHMs shown in Figure 5a were observed to increase after annealing, indicating that annealing at 1150°C did not improve overall crystal quality. As-implanted Sn samples had poorer FWHM values compared to the Si-implanted and annealed samples. The rocking curves were much larger than the intrinsic Darwin widths since they are implanted, as summarized in Table I. The intrinsic FWHM in arcsecs were 6.2 for the (−201) reflection, 3.5 for (−12,0,1), and 3.6 for (−11,1,1). These results show that more severe crystalline damage was induced by the implantation of Sn and Si, as expected by the larger size of the Sn ion, and was not completely removed after the 1150°C anneal.

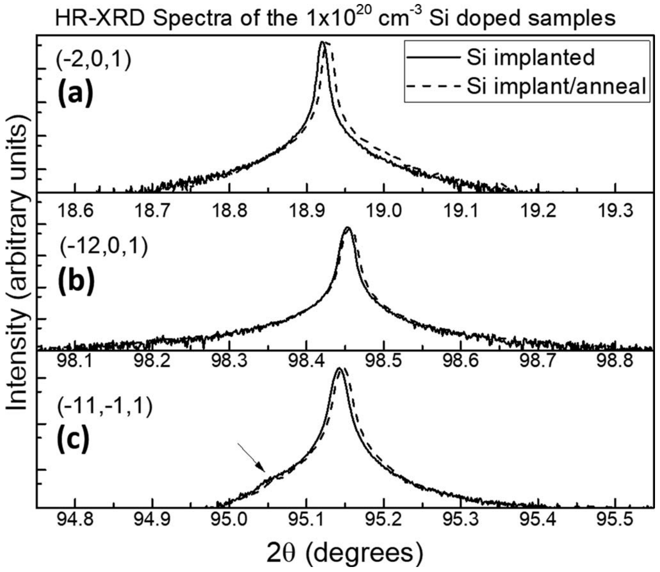

Figure 3. High resolution XRD spectra of the samples implanted with Si to an average concentration of 10^{20} cm^{-3}, both before and after annealing at 1150°C.

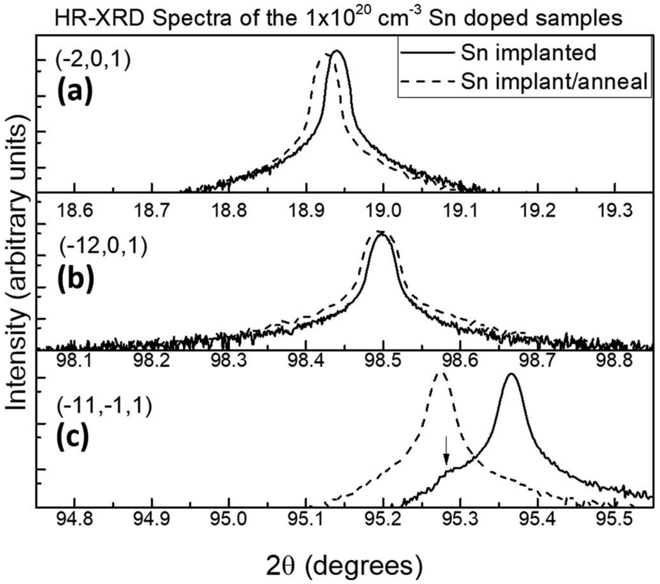

Figure 4. High resolution XRD spectra of the samples implanted with Sn to an average concentration of 10^{20} cm^{-3}, both before and after annealing at 1150°C.

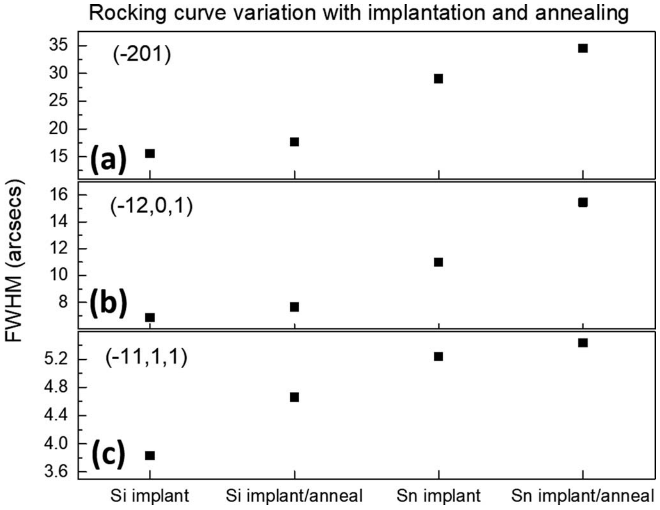

Figure 5. Variation of rocking curve FWHM after implantation and subsequent annealing for the samples implanted with Si or Sn to an average concentration of 10^{20} cm^{-3}. The annealing was performed at 1150°C.

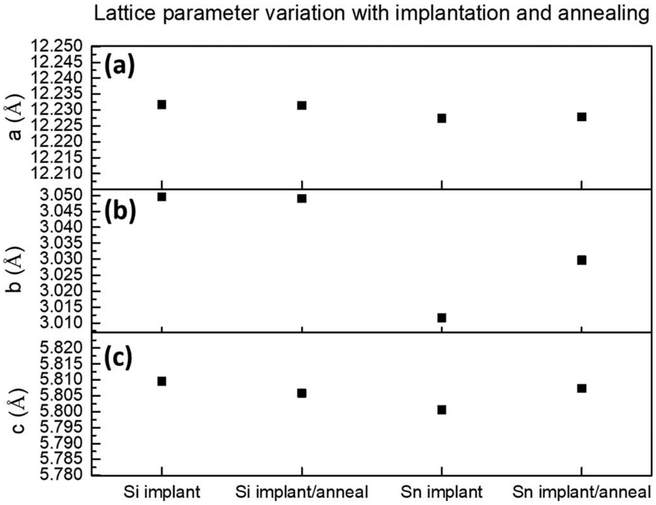

Figure 6. Variation of lattice parameters after implantation and subsequent annealing for the samples implanted with Si or Sn to an average concentration of 10^{20} cm^{-3}. The annealing was performed at 1150°C.

Selected area diffraction patterns from the Sn implanted samples before and after 1150°C annealing are shown in Fig. 7, indicating a significant improvement in crystalline quality in the implanted area upon annealing. The corresponding cross-section TEM images are shown at the top of Fig. 8. The end-of-range damage region in the as-implanted sample is centered at a depth of ∼114.5 nm from the surface, consisting of extended defects created by the nuclear collision energy loss during the ion stopping process. This region starts ∼76 nm from the surface. The 1150°C anneal is successful in removing this damage region (image at top right of Fig. 8). The high resolution images at the bottom of Fig. 8 shows the improved crystallinity of the annealed sample relative to the as-implanted state.

Previous CL and photoluminescence (PL) studies on Ga_2O_3 have shown fairly typical results with lack of near band-edge emissions, but most samples show consistently two or three emission bands near the UV (3.2–3.6 eV), blue (2.8–3.0 eV), and green (2.4 eV) spectral regions.[37–40] In nominally undoped EFG samples similar to those used here, Onuma et al.[40] reported that the UV emission bands at 3.2, 3.4 and 3.6 eV dominate at low temperatures, while at room temperature the blue (2.8 and 3 eV) and green (2.4 eV) bands were more prominent. Si-doped EFG samples showed only the UV bands.[40] Yamaga et al.[37] suggested that the blue emission occurs through recombination of self-trapped holes[41] and an electron trapped at a single oxygen vacancy.

Luminescence is a non-invasive and non-destructive technique widely employed to detect and identify native and impurity related point defects and their complexes in semiconductors. Especially in case of wide bandgap semiconductors, because of the large activation energies that are beyond the reach of conventional exciting light sources, CL has become the method of choice to investigate defects controlling the optical and optoelectronic properties of such materials.[42] Another advantage of CL spectroscopy is the depth-profiling capability, easily accessed by increasing the impinging electron-beam (E-beam) energy.[43] CL depth-profiling is extremely useful in the study of activation of implanted dopants, thermal annealing, and multi-layered structured materials. To verify its usefulness application in Ga_2O_3, we carry out low temperature (5K) CL measurements on as-implanted and implanted-annealed (010) samples with Si uniform concentration of 10^{20} cm^{-3}. Fig. 9a shows the presence of extremely weak emission bands in the spectra of the as-implanted sample acquired with 3 and 5 keV E-beam energies, in the spectral range between 1.5 and 5.0 eV. The unresolved and weak emission bands readily observed at ∼3.20 and ∼3.45 eV in the CL spectra excited with 7 keV E-beam becomes quite intense under 10 keV E-beam excitation. This clearly indicates that the implantation damage region, where the non-radiative and/or recombination process emitting outside of the probed region, is confined within the region accessed by E-beam accelerating voltage around 5 keV. Monte Carlo simulation, a numerical approach to estimate the final relative densities of electrons at the end of their secondary electrons multiplication and cascade, yields a Bohr-Bethe maximum range of 160 nm for 5 keV E-beam energy.[44] This value is consistent with the TEM cross-section imaging of implanted samples. The 5K CL spectra of the implanted-annealed sample, acquired with the same E-beam energies of the implanted samples represented in Fig. 9a, are depicted in Fig. 9b. The observation of relatively intense emission bands at ∼3.20 and ∼3.45 eV acquired with 3 and 5 keV E-beam energies indicates that the annealing procedure heals, at least partially, the implantation lattice damage. The ratio of the peak intensities of spectra measured in both samples with 7 keV and 10 keV are 126 and 85, respectively. The reduction of this ratio with increasing penetration depth confirms that the defects in the damaged layer strongly compete for the generated electron-hole pairs. Annealing experiments with un-implanted samples will be carried out to verify potential changes in the recombination rates involving intrinsic defects. It should be point out that the experiments will be carry out with an E-beam energy of 3 keV to probe only the samples implanted regions.

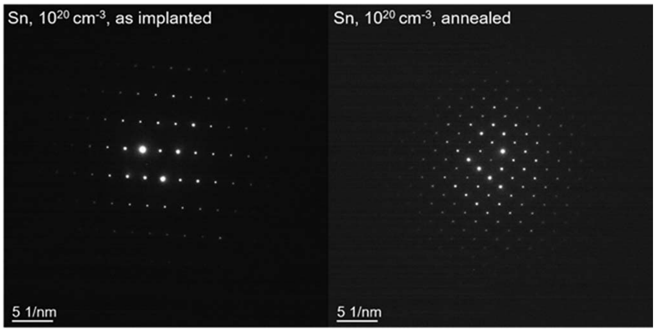

Figure 7. Selected area diffraction patterns from Sn-implanted (10^{20} cm^{-3} average concentration) Ga_2O_3 before (left) and after (right) annealing at 1150°C.

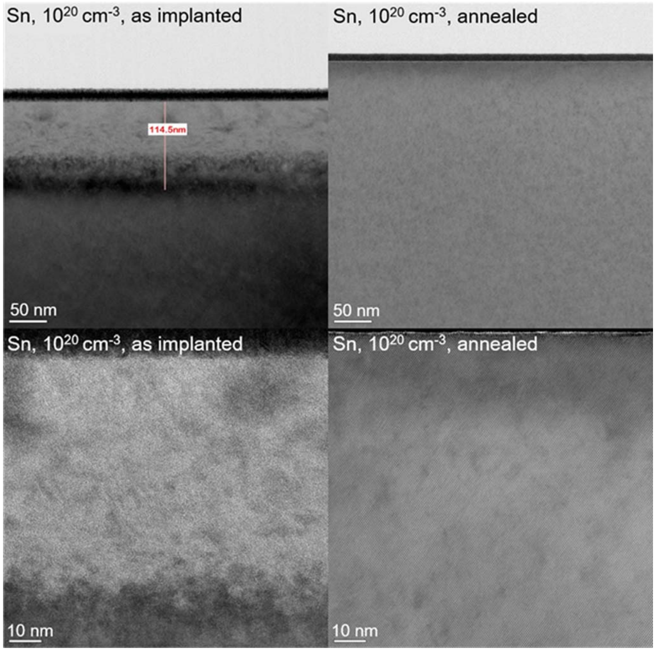

Figure 8. Cross-section TEM images of Sn-implanted (10^{20} cm^{-3}) Ga_2O_3 before (left, top and bottom) and after (right, top and bottom) annealing at 1150°C.

Figures 10a, 10b and 11a, 11b show the CL spectra of Si- and Sn-implanted (−201) samples (doses equivalent to an average volume

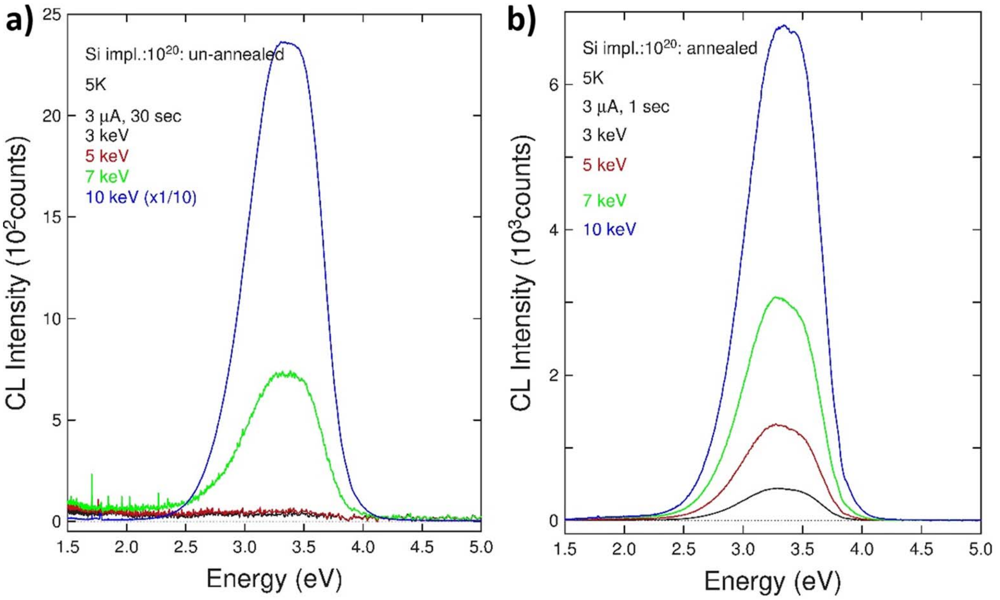

Figure 9. Depth-resolved CL spectra at 5 of Si-implanted (10^{20} cm^{-3}) Ga_2O_3 before and after annealing at 1150°C using 3–10 keV beam excitation energy.

concentration of 10^{20} cm^{-3}), before and after annealing at 1150°C, acquired at 297K and 5K, respectively. Differently from the (010) Si as-implanted sample, this two (−201) as-implanted samples show an "ambar" coloration, which are not observed after annealing procedure.[45] The absence of emission bands in the 297K spectrum of the as-implanted and the relatively large increase of the UV emission bands in the 297K spectra of the implanted/annealed sample, highlighted in Fig. 10a, indicate that non-radiative processes dominates recombination in the as-implanted sample. Similar trend is also observed in the spectra acquired at 5K, highlighted in Fig. 10b, despite the relatively small increase of the UV emission band peak intensity of the as-implanted sample spectrum. The 297K spectra of the Sn as-implanted and implanted/annealed samples are shown in Fig. 11a. Similar to the previous case, no emission was observed in the spectrum of the as-implanted sample, while a relatively high intensity near UV luminescence band is observed in the spectrum of the annealed sample. However, a new emission band ∼2.40 eV is observed in the latter spectrum. This emission band has been recently assigned to the presence of tetrahedrally coordinated Ga vacancies (V_{Ga}).[46] Note that, the near UV emission bands at ∼ 3.30 and ∼ 3.46 eV dominates the spectrum acquired at 5K. This clearly indicated that the 2.4 eV emission band has a different annealing and/or recombination-process temperature dependence from that of the near UV bands. The relatively large near UV emission peak intensity in the as-implanted sample spectrum resulted cracks in the film, which are introduced during cooling cycles, allowing partial probing of the un-implanted region below the implanted layer. The cracks on the film result from the different thermal expansion coefficients of the highly damage Sn-implanted layer and the pristine underneath substrate. These results are consistent with the XRD and TEM results that observed large structural damage by the Sn implantation.

We observed significant redistribution of the Si and Sn during annealing. The simulation of this diffusion was performed in the FLOOPS simulator,[33] via a Fick's diffusion based model. This model

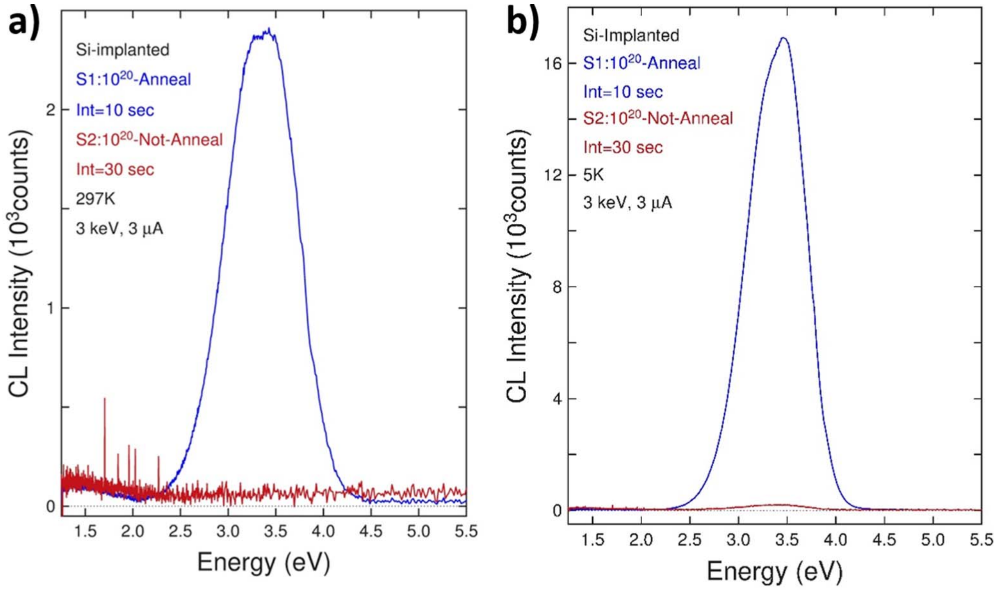

Figure 10. Room-temperature and 5 K CL spectra of Si-implanted (10^{20} cm^{-3}) Ga_2O_3 before and after annealing at 1150°C.

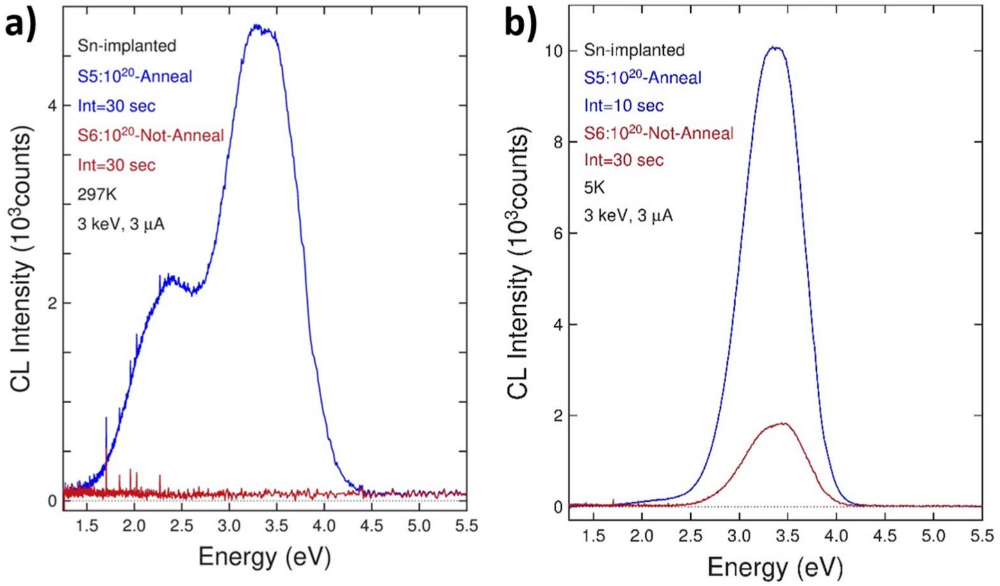

Figure 11. Room-temperature and 5 K CL spectra of Sn-implanted (10^{20} cm^{-3}) Ga_2O_3 before and after annealing at 1150°C.

included a concentration dependent diffusion factor and segregation to the surface.[33] The concentration dependent diffusion can be represented by the following equations:

$$D_o = [D + (D_D.C)]$$

$$\frac{dC}{dt} - D_o \frac{d}{dx}\,\frac{dC}{dx} = 0$$

where, D is the diffusing species diffusivity, D_D is the concentration dependent diffusion coefficient, C is the species concentration and D_o is the concentration dependent diffusivity. The surface segregation can be represented by;

$$K_s \cdot C = 0$$

where, K_s is the rate of loss to the surface of the diffusing species. In this case, there was no detectable loss of the dopant to the surface as determined the constancy of the integrated area under the dopant profiles before and after annealing. This is a factor for gaseous species like hydrogen and fluorine, but is not significant for Si and Sn.

The fits to the experimental SIMS profiles are shown in Figure 12 for Sn and Figure 13 for Si implantation, showing the as-implanted curves, with the experimental and fitted profiles after annealing, at 1150°C for 1 min. We achieved accurate fits for both Sn and Si profiles. For the sample implanted with Si, the SIMS measurements showed the presence of an interface at approximately 480 nm. This makes the Si calibration error larger in the region deeper than 480 nm. This can be seen in the experimental diffusion profiles, showing a steep drop at ~480 nm in the Si concentration, while the fit is not good at depths >480 nm. This suggests some change in the particle diffusivities or diffusion mechanism. The extracted diffusion coefficients are summarized in Table II. Note that the diffusivity of Si is almost an order of magnitude larger than that of Sn at 1150°C. It will be important to perform more detailed temperature and concentration-dependent diffusion studies to obtain the activation energies for these elements, as well as for Ge.

Table II. Diffusion-related parameters extracted from FLOOPS fitting of SIMS profiles.

Coefficient at 1150°C	Si	Sn
Diffusivity (D) cm.s^1	9.5×10^{-13}	1.68×10^{-13}
Conc. Dependent diff (D_D) cm.s^{-1}	8.0×10^{-31}	3.5×10^{-30}
Surf outgas rate (K_s)	8.0×10^{-8}	1.28×10^{-7}

Conclusions

For implant doses in the range 2×10^{13}–2×10^{15} cm^{-2} of the common donor species in Ga_2O_3, namely Si and Sn, annealing at 1150°C for 60 sec recovered the end-of-range damage visible in TEM and the CL intensity from the implanted region. The lattice parameters for Sn implants were not completely recovered under these conditions, indicating that higher annealing temperatures might be desirable for heavier implanted ion species. Both Si and Sn display significant redistribution during this annealing and their atomic profiles could be accurately fitted to a concentration-dependent diffusion model. None of the donors showed measurable activation above the existing

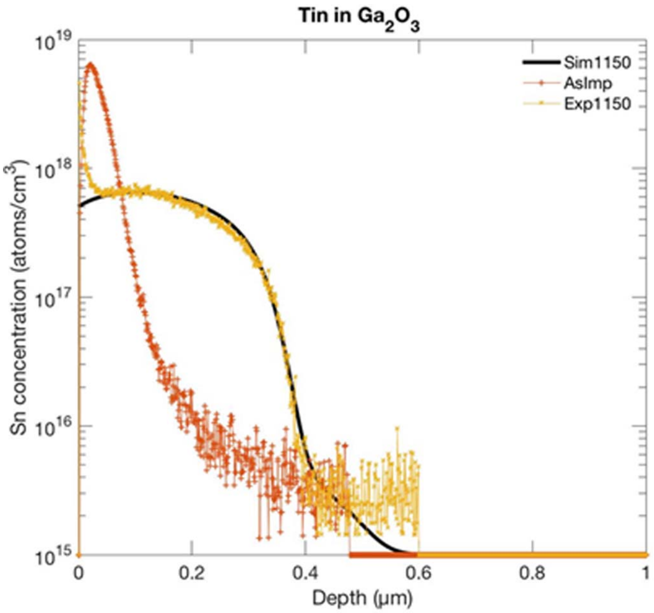

Figure 12. SIMS and simulated profiles of Sn-implanted Ga_2O_3 with a 10^{18} cm^{-3} total dose before and after annealing at 1150°C.

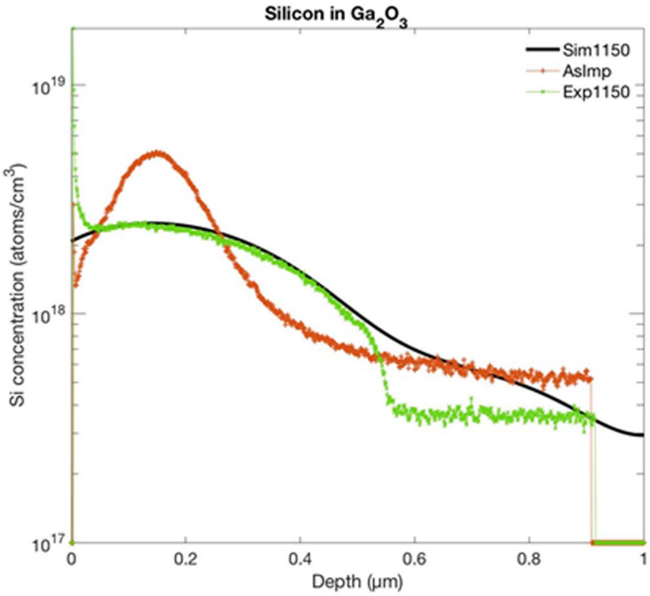

Figure 13. SIMS and simulated profiles of Si-implanted Ga_2O_3 with a 10^{18} cm^{-3} total dose before and after annealing at 1150°C.

background conductivity, indicating that lower compensation levels are needed to measure the activation kinetics. Meaningful activation studies will require thin, low-doped Ga_2O_3 epi on Mg-doped substrates to avoid diffusion of Fe from the substrate upon activation annealing.[47] Thicker HVPE epilayers might be acceptable as well since their background carrier concentration is typically lower than that of MBE-grown Ga_2O_3, as long as the influence of the non-implanted epi is corrected using a suitable multi-layer model.[48] Insulating Ga_2O_3 with lower densities of compensating acceptors, such as the recently reported Si/N compensated material, could be used as well.[16] However, such Ga_2O_3 material has not been demonstrated to-date.

Acknowledgments

Research at the NRL was supported by the Office of Naval Research (ONR). Research at Novel Crystal Technology was partially supported by ONR Global (grant No. N62909-16-1-2217). The work at UF was sponsored by the Department of the Defense, Defense Threat Reduction Agency, HDTRA1-17-1-011, monitored by Jacob Calkins. The content of the information does not necessarily reflect the position or the policy of the federal government, and no official endorsement should be inferred.

ORCID

Marko J. Tadjer https://orcid.org/0000-0002-2388-2937
Chaker Fares https://orcid.org/0000-0001-9596-2381
Ribhu Sharma https://orcid.org/0000-0001-5754-7873
Fan Ren https://orcid.org/0000-0001-9234-019X
S. J. Pearton https://orcid.org/0000-0001-6498-1256

References

1. M. Baldini, M. Albrecht, A. Fiedler, K. Irmscher, R. Schewski, and G. Wagner, *ECS Jour. Solid State Sci. Technol.*, **6**, Q3040 (2017).
2. H. von Wenckstern, *Adv. Electron. Mater.*, **3**, 1600350 (2017).
3. M. Higashiwaki, K. Sasaki, H. Murakami, Y. Kumagai, A. Koukitu, and A. Kuramata, *Semicond. Sci. Technol.*, **31**, 034001 (2016).
4. S. J. Pearton, J. Yang, P. H. Cary, F. Ren, J. Kim, and M. J. Tadjer, *Appl. Phys. Rev.*, **5**, 011301 (2018).
5. Zbigniew Galazka, *Semicond. Sci. Technol.*, **33**, 113001 (2018).
6. A. Kuramata, K. Koshi, S. Watanabe, Y. Yamaoka, T. Masui, and S. Yamakoshi, *Jpn. J. Appl. Phys.*, **55**, 1202A2 (2016).
7. Marko J. Tadjer, Nadeemullah A. Mahadik, Jaime A. Freitas Jr., Evan R. Glaser, Andrew Koehler, Lunet E. Luna, Boris N. Feigelson, Karl D. Hobart, Fritz J. Kub, and A. Kuramata, *Proc. of SPIE*, **10532**, 1053212 (2018).
8. Z. Hu, K. Nomoto, W. Li, N. Tanen, K. Sasaki, A. Kuramata, T. Nakamura, D. Jena, and H. G. Xing, *IEEE Electron Dev. Lett.*, **39**, 869 (2018).
9. S. Rafique, L. Han, A. T. Neal, S. Mou, M. J. Tadjer, R. H. French, and H. Zhao, *Appl. Phys. Lett.*, **109**, 132103 (2016).
10. E. Ahmadi, O. S. Koksaldi, S. W. Kaun, Y. Oshima, D. B. Short, U. K. Mishra, and J. S. Speck, *Appl. Phys.*, **7**(10), 041102 (2017).
11. K. Sasaki, M. Higashiwaki, A. Kuramata, T. Masui, and S. Yamakoshi, *Appl. Phys. Expr.*, **6**, 086502 (2013).
12. M. H. Wong, C.-H. Lin, A. Kuramata, S. Yamakoshi, H. Murakami, Y. Kumagai, and M. Higashiwaki, *Appl. Phys. Lett.*, **113**, 102103 (2018).
13. E. Nogales, P. Hidalgo, K. Lorenz, B. Mendez, J. Piqueras, and E. Alves, *Nanotechnology*, **22**, 285706 (2011).
14. S.-H. Han, A. Mauze, E. Ahmadi, T. Mates, Y. Oshima, and J. S. Speck, *Semicond. Sci. Technol.*, **33**, 045001 (2018).
15. S. D. Lee, K. Kaneko K, and S. Fujita, *Japan. J. Appl. Phys.*, **55**, 1202B8 (2016).
16. Marko J. Tadjer, Andrew D. Koehler, Jaime A. Freitas, James C. Gallagher, Matty C. Specht, Evan R. Glaser, Karl D. Hobart, Travis J. Anderson, Fritz J. Kub, Quang T. Thieu Kohei Sasaki, Daiki Wakimoto, Ken Goto, Shinya Watanabe, and Akito Kuramata, *Appl. Phys. Lett.*, **113**, 192102 (2018).
17. T. Onuma, Y. Nakata, K. Sasaki, T. Masui, T. Yamaguchi, T. Honda, A. Kuramata, S. Yamakoshi, and M. Higashiwaki, *J. Appl. Phys.*, **124**, 075103 (2018).
18. Kornelius Tetzner, Andreas Thies, Eldad Bahat Treidel, Frank Brunner, Günter Wagner, and Joachim Würfl, *Appl. Phys. Lett.*, **113**, 172104 (2018).
19. M. H. Wong, Y. Nakata, A. Kuramata, S. Yamakoshi, and M. Higashiwaki, *Appl. Phys. Express*, **10**, 041101 (2017).
20. M. H. Wong, K. Goto, Y. Morikawa, A. Kuramata, S. Yamakoshi, H. Murakami, Y. Kumagai, and M. Higashiwaki, *Appl. Phys. Express*, **11**, 064102 (2018).
21. Man Hoi Wong, Chia-Hung Lin, Akito Kuramata, Shigenobu Yamakoshi, Hisashi Murakami, Yoshinao Kumagai, and Masataka Higashiwaki, *Appl. Phys. Lett.*, **113**, 102103 (2018).
22. A. Y. Polyakov, N. B. Smirnov, I. V. Shchemerov, S. J. Pearton, Fan Ren, A. V. Chernykh, and A. I. Kochkova, *Appl. Phys. Lett.* **113**, 142102 (2018).
23. J. F. McGlone, Z. Xia, Y. Zhang, Chandan Joishi, S. Lodha, S. Rajan, S. A. Ringel, and A. R. Arehart, *IEEE Electron. Dev. Lett.*, **39**, 1042 (2018).
24. K. Irmscher, Z. Galazka, M. Pietsch, R. Uecker, and R. Fornari, *J. Appl. Phys.*, **110**, 063720 (2011).
25. Adam T. Neal, Shin Mou, Subrina Rafique, Hongping Zhao, Elaheh Ahmadi, James S. Speck, Kevin T. Stevens, John D. Blevins, Darren B. Thomson, Neil Moser, Kelson D. Chabak, and Gregg H. Jessen, *Appl. Phys. Lett.*, **113**, 062101 (2018).
26. Z. Zhang, E. Farzana, A. R. Arehart, and S. A. Ringel, *Appl. Phys. Lett.*, **108**, 052105 (2016).
27. M. E. Ingebrigtsen, J. B. Varley, A. Yu. Kuznetsov, B. G. Svensson, G. Alfieri, A. Mihaila, U. Badstübner, and L. Vines, *Appl. Phys. Lett.*, **112**, 042104 (2018).
28. J. C. Zolper, J.C., *J. Cryst. Growth*, **178**, 157 (1997).
29. K. Hoshikawa, E. Ohba, T. Kobayashi, J. Yanagisawa, C. Miyagawa, and Y. Nakamura, *J. Cryst. Growth*, **447**, 36 (2016).
30. R. Togashi, K. Nomura, C. Eguchi, T. Fukizawa, K. Goto, Q. T. Thieu, H. Murakami, Y. Kumagai, A. Kuramata, and S. Yamakoshi, *Japan. J. Appl. Phys.*, **54**, 041102 (2015).
31. W. Mu, Z. Jia, Y. Yin, Q. Hu, Y. Li, B. Wu, J. Zhang, and X. Tao, *J. Alloys Comp.*, **714**, 453 (2017).
32. V. I. Nikolaev, V. Maslov, S. Stepanov, A. Pechnikov, V. Krymov, L. Nikitina, L. Guzilova, V. Bougrov, and A. A. Romanov, *J. Cryst. Growth*, **457**, 132 (2017).
33. http://www.flooxs.tec.ufl.edu/.
34. S. Geller, *J. Chem. Phys.*, **33**, 676 (1960).
35. J. Åhman, G. Svensson, and J. Albertsson, *Acta Crystallogr.* **C52**, 1336 (1996).
36. H. Peelaers and C. G. Van de Walle, *Phys. Status Solidi B*, **252**(4), 828 (2015).
37. M. Yamaga, T. Ishikawa, M. Yoshida, T. Hasegawa, E. G. Villora, and K. Shimamura, *Phys. Status Solidi c*, **8**, 2621 (2011).
38. K. Shimamura, E. G. Víllora, T. Ujiie, and K. Aoki, *Appl.Phys. Lett.*, **92**, 201914 (2008).
39. S. Yamaoka and M. Nakayama, *Phys. Status Solidi C*, **13**, 93 (2016).
40. T. Onuma, S. Fujioka, T. Yamaguchi, M. Higashiwaki, K. Sasaki, T. Masui, and T. Honda, *Appl. Phys. Lett.*, **103**, 041910 (2013).
41. J. B. Varley, A. Janotti, C. Franchini, and C. G. Van de Walle, *Phys. Rev. B*, **85**, 081109 (2012).
42. J. A. Freitas Jr., *J. Crystal Growth*, **281**, 168 (2005).
43. E. Silveira, J. A. Freitas Jr., G. A. Slack, L. J. Schowalter, M. Kneissl, D. W. Treat, and N. M. Johnson, *J. Crystal Growth*, **281**, 188 (2005).
44. P. Hovington, D. Drouin, and R. Gauvin, "CASINO": A new Monte Carlo code in C Language for electron beam interaction", *Scanning*, **19**, 1 (1997).
45. J. A. Freitas Jr. et al., 2nd Intl. Workshop on Ga_2O_3, Parma, Italy, 2017.
46. B. E. Kananen, L. E. Halliburton, K. T. Stevens, G. K. Founds, and N. C. Giles, *Appl. Phys. Lett.*, **110**, 202104 (2017).
47. M. H. Wong, K. Sasaki, A. Kuramata, S. Yamakoshi, and M. Higashiwaki, *Appl. Phys. Lett.*, **106**, 032105 (2015).
48. O. Bierwagen, S. Choi, and J. S. Speck, *Phys. Rev. B*, **84**, 235302 (2011).